Research Article Vol. 36, No. 9 / September 2019 / Journal of the Optical Society of America B 2587

Journal of the Optical Society of America B

OPTICAL PHYSICS

Digital sensor based on multicavity fiber interferometers

Ubaid Ullah,[1] Muhammad Yasin,[2] Alper Kiraz,[3] and M. Imran Cheema[1,*]

[1]Department of Electrical Engineering, Syed Babar Ali School of Science and Engineering, LUMS, Sector U, DHA, Lahore, Pakistan
[2]Department of Physics, Syed Babar Ali School of Science and Engineering, LUMS, Sector U, DHA, Lahore, Pakistan
[3]Department of Physics and the Department of Electrical and Electronics Engineering, Koc University, Istanbul 34450, Turkey
*Corresponding author: imran.cheema@lums.edu.pk

Received 31 May 2019; accepted 5 August 2019; posted 8 August 2019 (Doc. ID 368923); published 27 August 2019

Vernier effect systems with more than two reflectors or coupled-ring resonators are highly attractive for sensing applications, since one can have better control of tailoring their transmission response as compared to traditional single-cavity structures. Here, we propose and provide a prescription for designing a digital Vernier sensor that can be built from three off-the-shelf fiber Bragg gratings. The proposed sensor employs a tapered fiber in one of the cavities as a sensing head and senses changes in the form of discrete (digital) wavelength jumps of resonant modes. We show that the sensitivity, detection limit, and dynamic range of the sensor can be predictably controlled by careful selection of cavity lengths. As an example, we show by simulations that the detection limit of the proposed sensor reaches 10^{-6}, which is eight times more than the previously proposed digital sensor based upon coupled-ring resonators.

https://doi.org/10.1364/JOSAB.36.002587

1. INTRODUCTION

In the last few years, Fabry–Perot interferometer (FPI)-based optical sensors have been widely investigated for numerous applications, including pressure [1], strain [2], temperature [3], gasses [4], and humidity measurements [5]. In FPI sensing applications, researchers always desire to have high sensitivity, dynamic range, and detection limit. One way of increasing the performance of FPI sensors is to exploit the Vernier effect in a multicavity configuration [6].

Vernier-effect-based multicavity sensors have been previously proposed in various optical fibers [7–9] and in ring resonators [10–13]. In multicavity sensing works, researchers have looked over two regimes for their sensing applications. These include tracking of (i) continuous frequency shifts in the FPI transmission envelope [7–12] for various sensing schematics and (ii) discrete frequency shifts (digital) in individual resonant peaks of coupled-ring resonators [13]. The digital sensing scheme is appealing due to the potential of achieving ultralow detection limits. In a previous work, researchers proposed two cascaded-ring resonators with slightly different free spectral ranges (FSRs) for realizing a digital sensor [13]. In that work, deterministic control of dynamic range, sensitivity, and detection limit as a function of rings' parameters was not quantitatively explored. The digital sensing with ring resonators is also somewhat challenging due to tight fabrication tolerances on parameters of microrings and coupling waveguides [13]. In our work, we provide a comprehensive prescription for designing digital multicavity FPI sensors with high performance by employing off-the-shelf fiber Bragg gratings (FBG). The FSR of our proposed two-cavity sensor plays an important role in determining its dynamic range, sensitivity, and detection limit. Therefore, starting with the well-known matrix method result of the three-mirror cavity [14], we analyze and provide a simple physical interpretation of the obtained transmission response as a function of cavity lengths and reflectivities. We also provide an analytical expression of FSR for our sensing needs.

We propose to build the two-cavity sensor from three FBGs. We propose to use a current-tuned distributed feedback (DFB) laser and photodetector to track the sensor's transmission spectrum as a function of sensing events. A tapered fiber is inserted in one of the two cavities and acts as a sensing head. The lengths of two cavities are adjusted such that it follows our derived FSR expression.

The proposed system's potential as a refractive index (RI) sensor is then analyzed via simulations. We find that RI changes induce discrete frequency shifts (digital sensing) of resonant peaks in the sensor's transmission response. We then analyze the detection limit and sensitivity of the sensor as a function of the lengths of two cavities in the sensor. The two lengths are picked in such a deterministic way that all combinations produce not only systematic digital shifts but also the same FSR as predicted by our derived equation. As an example, we show via simulations that the proposed sensor produces the dynamic range, sensitivity, and detection limit of 2.4×10^{-5} RIU, 314 nm/RIU,

and 10^{-6} RIU, respectively, for the FSR of 8.31 pm. The achieved detection limit is eight times more than that of the previously demonstrated digital sensor based upon coupled-ring resonators [13].

We now describe the rest of the paper. In Section 2, we analyze transmission of the two-cavity FPI and provide an expression for its FSR. In Section 3, we propose and design the two-cavity digital FPI sensor based upon our derived FSR expression. In the same section, we also look over sensitivity and minimum detection limit of the proposed sensor as a function of design parameters. We provide discussion on the obtained results in Section 4. Finally, we provide discussion on the obtained results and concluding remarks in Section 5.

2. FSR EXPRESSION FOR A TWO-CAVITY FPI

Consider an FPI composed of three reflectors as shown in Fig. 1. The FPI transmission is given by [14]

$$T = \frac{(t_1 t_2 t_3)^2}{D}, \tag{1}$$

where

$$\begin{aligned} D =& 1 + (r_1 r_2)^2 + (r_2 r_3)^2 + (r_1 r_3)^2 + 2 r_1 r_2 (1 + r_3^2) \cos(2\phi_1) \\ &+ 2 r_2 r_3 (1 + r_1^2) \cos(2\phi_2) + 2 r_1 r_3 \cos(2\phi_1 + 2\phi_2) \\ &+ 2 r_1 r_2^2 r_3 \cos(2\phi_1 - 2\phi_2), \end{aligned} \tag{2}$$

where r_i and t_i $(i = 1, 2, 3)$ are amplitude reflection and transmission coefficients of reflectors, respectively, and $\phi_i = \frac{2\pi n_i L_i}{\lambda}$ $(i = 1, 2)$ are phase lengths of two cavities.

The reflectivity, R_2, will play a pivotal role in determining the transmission response of this multicavity FPI. Intuitively, one can think that if R_2 is closer to 1, then the two cavities, $R_1 L_1 R_2$ and $R_2 L_2 R_3$, will be negligibly coupled to each other. However, as R_2 starts decreasing, the two cavities will begin to couple with each other, and when R_2 becomes 0, then we will have the standard FPI with two reflectors, $R_1 L_1 L_2 R_3$.

From Eq. (1) it is clear that the transmission, T, is maximum whenever D [Eq. (2)] is minimum. Considering the case of $R_2 \geq 0.99$, one can easily see that by taking the ratio of individual terms, the fifth and sixth terms of D are the dominant ones. In other words, if sinusoids in both fifth and sixth terms are at their negative peaks, then the maximum transmission will occur. Therefore, for the transmission peak, one requires

$$\phi_1 = \frac{(2n+1)\pi}{2}, \tag{3}$$

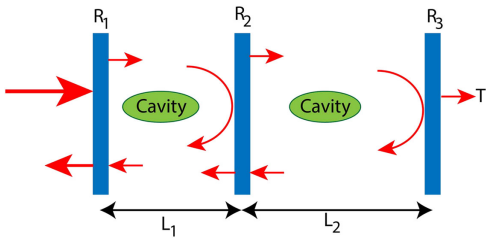

Fig. 1. Schematics of an FPI composed of three reflectors.

$$\phi_2 = \frac{(2m+1)\pi}{2}, \tag{4}$$

where $m = 0, 1, 2, 3, \ldots$ and $n = 0, 1, 2, 3, \ldots$. Intuitively, one needs to look at the behavior of just $\cos 2\phi_1$ and $\cos 2\phi_2$ to understand and predict the transmission response. For convenience and without the loss of generality, one can assume that

$$\phi_2 = M\phi_1, \tag{5}$$

where $M = \frac{n_2 L_2}{n_1 L_1}$ and is a positive real number. Since Eq. (2) remains the same if we replace R_1 and L_1 with R_3 and L_2, respectively, we can also assume that $L_2 \geq L_1$ without the loss of generality. By using Eqs. (3)–(5), we obtain the maximum transmission condition:

$$m = \frac{2Mn + M - 1}{2}. \tag{6}$$

Note that m and n *have to be* integers, and M *can be* any positive real number in Eq. (6) for achieving maximum transmission. Let us now consider different cases for M.

A. *M* Is an Even or Odd Integer

From Eq. (6), one can clearly see that for an even M, there will never be an integral value of m, and hence no transmission maxima will exist; however, for an odd M transmission, maxima will always exist. Physically, each integral value of n and m corresponds to negative peaks of $\cos(2\phi_1)$ and $\cos(2M\phi_1)$, respectively. Mathematically, one can also readily verify that whenever $\cos(2\phi_1)$ and $\cos(2M\phi_1)$ are at their negative peaks, then $\cos(2\phi_1 + 2M\phi_1)$ [seventh term of Eq. (2)] and $\cos(2\phi_1 - 2M\phi 1)$ [eighth term of Eq. (2)] are at their positive peaks for an odd integer M. In the case of an even integer M, there will be no overlapping peaks of the two dominant sinusoids [fifth and sixth terms of Eq. (2)] and hence no transmission maxima. Using Eq. (3), we can deduce that the FSR, defined as the wavelength spacing between two maximum transmission modes, for an odd M will always be

$$\mathrm{FSR} = \frac{\lambda^2 M}{2 n_c L_2} = \frac{\lambda^2}{2 n_c L_1}, \tag{7}$$

where n_c is the RI of the fiber.

B. Non-Integer *M*

Considering the case of a non-integer M of the form

$$M = \frac{a}{b}, \tag{8}$$

this means that $a\phi_1 = b\phi_2$. If a and b are a combination of even and odd integers, then there will never be a perfect overlap of the negative peaks. However, one can find certain values of a and b, for which m can lie within ± 0.05 of an integer value. In this case, the FSR will increase significantly and form the basis of sensors based upon detecting shifts in the envelope of the overall FPI transmission [7–11].

If a and b are odd integers, then based upon discussions in Section 2.A, it is clear that $\cos(2\phi_1)$ and $\cos(2M\phi_1)$ will always

overlap at their negative peaks. Mathematically, values of n that can generate integer m values satisfy the following relation:

$$n = \alpha b + \frac{b-1}{2}, \tag{9}$$

where $\alpha = 0, 1, 2, \ldots$ represent absolute numbers of those negative peaks of $\cos(2\phi_1)$ that fully overlap with $\cos(2M\phi_1)$. Equation (9) is derived by determining the sequence for n that will make m [Eq. (6)] an integer for various M's. Substitution of Eq. (9) into Eq. (6) will generate an expression for the corresponding integral values of m and is given by

$$m = \alpha a + \frac{a-1}{2}. \tag{10}$$

One can clearly see that Eqs. (9) and (10) always produce integer values for odd a and b. The FSR in terms of ϕ_1 and ϕ_2 are simplified to $a\pi$ and $b\pi$, respectively. The FSR in terms of lengths of the two cavities is given by

$$\mathrm{FSR} = \frac{\lambda^2 a}{2n_c L_2} = \frac{\lambda^2 b}{2n_c L_1}. \tag{11}$$

This equation shows that the FSR is b times lager than that of the odd integer M case [Eq. (7)]. A representative case for $M = \frac{5}{3}$ is shown in Fig. 2, in which it is clear that the FSR is 3π as predicted. It should be noted that the same results will hold even if a and b transform to even numbers on multiplication with a common multiplier. However, in that case, a and b in Eq. (11) still represent odd integers in their lowest forms. Our work in the following sections on digital sensors will be using Eq. (11) as one of its key parameters.

Equation (11) is valid when reflectivities lie in the range $0.1 \lessapprox R_1, R_2 \lessapprox 0.85$, $R_2 \lessapprox 0.99$. When R_2 becomes less than 0.99, then intuitively one can think that the two cavities start to couple with each other. This means that, regardless of the value of M, the transmission maxima start to appear near the negative maxima of $2r_1 r_3 \cos(2\phi_1 + 2M\phi_1)$ [see Eqs. (1) and (2)]. As R_2 approaches zero, the transmission maxima will be exactly at negative peaks of $\cos(2\phi_1 + 2M\phi_1)$, i.e., we will approach the case of a single cavity with R_1 and R_3 as two reflectors. As R_1 or R_3 approaches zero, the system will approach a single cavity made up of $R_2 L_2 R_3$ or $R_1 L_1 R_2$, respectively. Consequently, the transmission maxima will start appearing at negative peaks of $\cos(2M\phi_1)$ or $\cos(2\phi_1)$, respectively. When R_1 becomes greater than 0.85, then the transmission not only reduces but also the peaks start to split. On the other hand, for $R_3 > 0.85$, secondary transmission peaks start to appear near all negative peaks of $\cos(2M\phi_1)$. One also finds that the effect of increasing of R_1 can be somewhat mitigated by decreasing R_3 and vice versa.

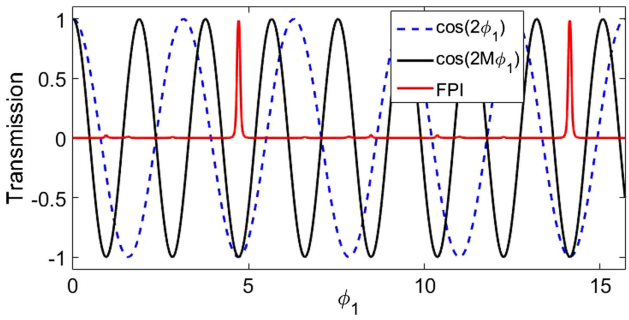

Fig. 2. FPI transmission [Eq. (1)] for $M = \frac{a}{b}$ with a, b odd integers. The FSR is b times more than the odd integer M case. Here, $M = \frac{5}{3}$, $R_1 = R_3 = 0.8$, and $R_2 = 0.99$.

3. DIGITAL FIBER FPI SENSOR

A. Design

The proposed schematic for the digital sensor built from three FBGs is shown in Fig. 3. A tapered fiber of waist diameter 1 μm and length, L_t, of 2 cm is inserted into one of the cavities as the sensing head. Let us consider that $M = \frac{5}{3}$ for $L_1 = 30$ cm and $L_2 = 50$ cm for our starting design. According to Eq. (11), this provides us the FSR of 8.31 pm. We assume that $n_c = 1.445$ for SMF-28 fiber. One can easily conclude that we can get the same FSR of 8.31 pm for various values of M, L_1, and L_2. However, the cavity lengths are selected such that the following updated condition for M is satisfied:

$$M = \frac{n_c L_2}{n_c(L_1 - L_t) + n_t L_t} = \frac{2\beta K \pm 1}{K}, \tag{12}$$

where K is any odd integer greater than 1, $\beta = 1, 2, 3, \ldots$, n_c, and n_t are effective indices of modes propagating in the SMF-28 and tapered fibers, respectively. Note that Eq. (12) is a subset of Eq. (8) when a and b are both odd integers. For example, $M = \frac{19}{11}$ can provide the desired FSR per Eq. (11) but does not satisfy Eq. (12) and hence will not provide a clear digital sensor response as explained below.

The condition in Eq. (12) makes sure that transmission modes of the two cavities are symmetrically separated from each other leading to a digital response of the proposed sensor with a similar trend for any value of K. This is illustrated in Fig. 4. The figure is produced under the assumption that the tapered fiber is immersed in water. The distance between each consecutive mode of the shorter cavity and alternative modes of the larger cavity follows an arithmetic sequence $Y, 2Y, 3Y, \ldots, \ell Y$, where

$$Y = \left| \frac{2\beta}{2K \pm 1} - \frac{1}{K} \right| \times \mathrm{FSR}. \tag{13}$$

A progressive sequence of signals will not be produced for M's that do not satisfy Eq. (12), as shown in Fig. 5. The shorter cavity modes (red plot) will slide forward and overlap with the larger cavity modes (blue plot) and produce back and forth transmission wavelength jumps as a function of sensing events. Consequently, in general, the sensor response will follow a

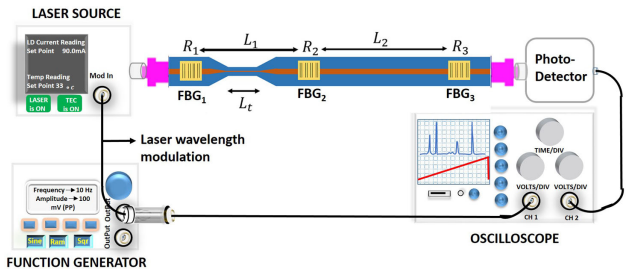

Fig. 3. Schematics of the proposed digital sensor.

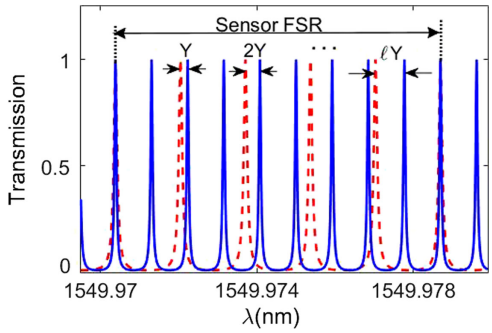

Fig. 4. Transmission peaks of individual cavities for $\beta = 1$, $K = 5$, i.e., $M = \frac{9}{5}$. The blue solid plot represents transmission modes of the larger cavity, while the red dashed graph shows smaller cavity modes.

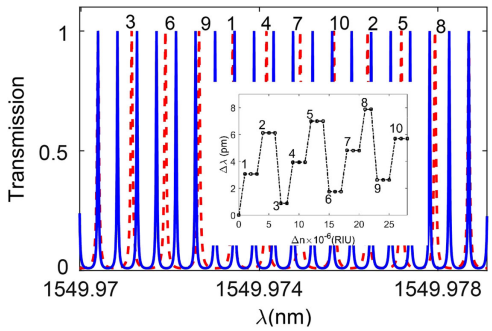

Fig. 5. Transmission peaks of individual cavities for $M = \frac{19}{11}$. 1, 2, ..., 10 signify the sequence of overlapping of modes. The inset shows wavelength changes in the sensor transmission (when the red and blue modes overlap) as a function of refractive index changes.

different trend for any value of M that does not satisfy Eq. (12). A representative example for $M = \frac{19}{11}$ is shown in Fig. 5. For the rest of the paper, we use those values of M that satisfy Eq. (12).

B. Simulation Results

In the previous section, we see that various values of K are possible for realizing the proposed digital sensor. In this section, we find optimum values of K that will produce the maximum sensitivity and detection limit for a given FSR.

In simulations, we assume three FBGs with reflectivities of $R_1 = R_3 = 0.82$, $R_2 = 0.99$ at the central wavelength of 1550 nm. We also consider the single-mode tapered fiber of 1 μm waist diameter and length, L_t, of 2 cm as the sensing surface in the shorter cavity. According to Eq. (11) if $\frac{a}{L_2} = \frac{b}{L_1}$ for different values of L_1 and L_2, then the FSR will remain constant. Therefore, we adjust the two lengths (L_1, L_2) to make sure that the aforementioned condition is satisfied to have the constant FSR of 8.31 pm for all values of K assumed in our simulations. We also assume $\beta = 1$ and subtraction in the numerator of Eq. (12) for all simulations.

During the modeling, we assume that the tapered fiber is immersed in water. We calculate the modal effective index of the immersed tapered fiber by finite element simulations (FEM). The sensor performance is then analyzed by introducing a small change in the RI of water and investigating the corresponding change in the transmission spectrum. The effective index of the single-mode tapered fiber, n_t, is recalculated using the FEM for each RI change around its surroundings.

In Fig. 4, it is clear that when RI changes are introduced in the vicinity of the tapered fiber, transmission modes of the shorter cavity will start sliding and overlap with larger cavity modes to produce a transmission maximum of the sensor in steps of Y [Eq. (13)]. As the RI changes from 0, transmission maxima will follow the previously mentioned sequence, and hence a digital sensing response will be produced. We keep on tracking the maximum transmission peak of the proposed two-cavity sensor as a function of RI changes. The peak changes its position discretely along the wavelength axis as shown in Fig. 6.

To further investigate the potential and characteristics of the proposed sensor, the peak position is tracked for different values of K as shown in Fig. 7. An increase in K increases the lengths of cavities, which in turn increases the number of individual cavity modes in the fixed system FSR of 8.31 pm. Thus, the number of discrete jumps in the overall system FSR increases. Consequently, the minimum detection limit of the sensor increases as shown in Fig. 8. It should be noted that we are using 1×10^{-6} as the RI step size in our simulations, and we reach this simulation limit for $K = 27$. As a reminder, we have generated results in Figs. 6 and 7 by using Eq. (1) while satisfying Eqs. (11) and (12).

The sensitivity results of the proposed sensor are shown in Fig. 9. The sensitivity for each value of K is calculated by dividing the wavelength shift required for the corresponding minimum detectable RI change [12]. The sensitivity curve can be understood in the light of Fig. 8, in which an increase in K

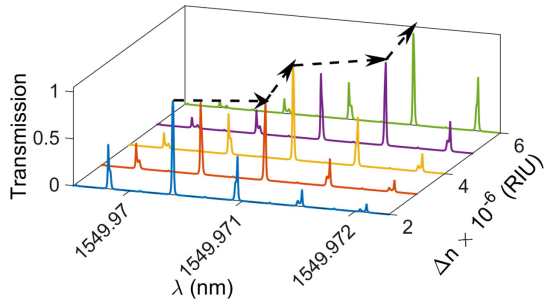

Fig. 6. Tracking the highest transmission peak for $K = 15$ as a function of RI changes. The discrete peak jumps are clearly visible.

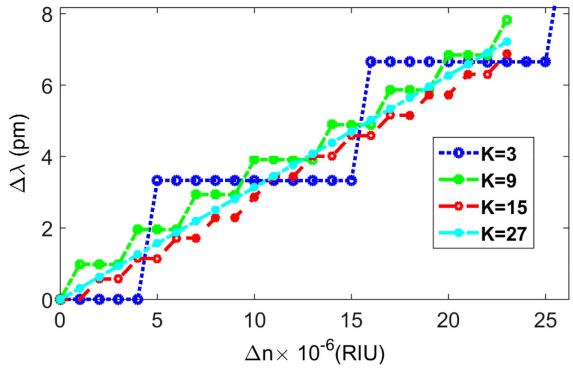

Fig. 7. Comparison between digital responses of sensor for different values of K.

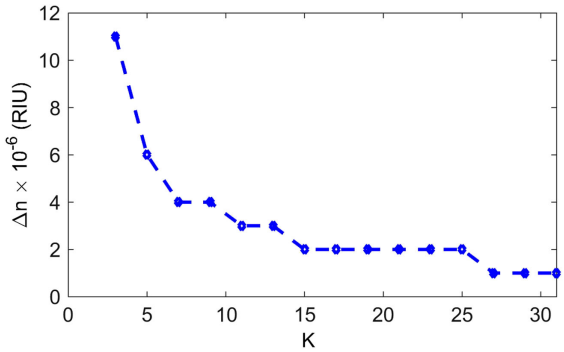

Fig. 8. Minimal detectable RI change as a function of the sensor parameter K.

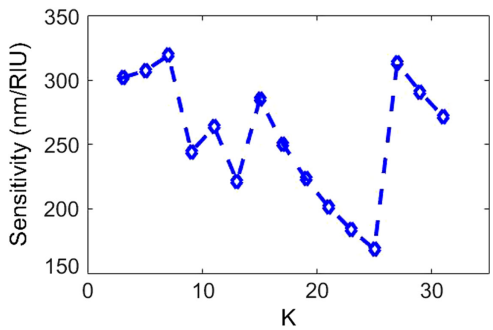

Fig. 9. Sensitivity as a function of the sensor parameter K.

may or may not improve the detection limit. For example, for $K = 3, 5, 7$, the decrease in detection limit improves the sensitivity, while for $K = 9$, no improvement in the detection limit worsens the sensitivity. It should be noted that an increase in K decreases Y [Eq. (13)] and hence the sensor's wavelength shift, $\Delta\lambda$, which is also evident in Fig. 7. Therefore, overall sensitivity is primarily dictated by the detection limit.

In Fig. 9, it is clear that although the maximum sensitivity of 320 nm/RIU is achieved at $K = 7$, the detection limit is lower at this K. For both high sensitivity and detection limit, one would like to operate the proposed sensor at $K = 27$. The FSR of the sensor is 8.31 pm, which corresponds to the dynamic range of 2.4×10^{-5} RIU.

4. DISCUSSION

Our results indicate that a high-performing multicavity sensor can be demonstrated with the help of a laser, photodetector, and off-the-shelf FBGs. The proposed sensor works on the principle of digital sensing as evident in Fig. 7. The sensor performance improves with an increase in K, which is analogous to classical digital systems where their performance also improves with an increase in quantization levels. Here, the number of cavity modes provides quantization levels that increase with an increase in K, as can be deduced from Eqs. (11) and (12). This effect is also clearly visible in Fig. 7 where staircase trends with lower values of K start becoming continuous as K increases. However, it should be noted that we see a continuous trend at $K = 27$ at the chosen step size of 10^{-6} RIU, which will be converted to a staircase trend as the RIU step size is further reduced. This indicates that we can detect $<10^{-7}$ RI changes with the proposed sensor. The lowest detection limit will be eventually dictated by the overall sensor measurement noise, which can be less than 20 fm for a DFB laser and photodetector-enabled sensing modality [15]. Note that our simulations indicate that it is required to detect $\Delta\lambda$ of 314 fm for measuring 10^{-6} RIU changes at $K = 27$.

In the present work, we are providing an example of centimeter-scale cavities due to the intended usage of off-the-shelf FBGs. However, the proposed sensor's performance will be enhanced in proportion if the length scales of two cavities are changed to millimeters or micrometers while respecting Eqs. (11) and (12).

One of the important aspects of the proposed two-stage fiber sensor is its FSR, which can be predictably increased by proper selection of cavity lengths as shown by Eqs. (11) and (12). These equations provide us guidelines to build the two-cavity FPI with a desired FSR from three off-the-shelf FBGs, as we just need to join the FBGs with selected fiber lengths. It should be noted that the maximum increase in FSR, with centimeter-scale cavity lengths, is limited by the tolerable intensity of undesired transmission modes in the designed FSR. Although this restriction can be removed by adding more FBGs, in that case, we need to re-derive Eqs. (11) and (12) for the desired number of cavities in the sensor.

5. CONCLUSION

We show that a digital sensor based upon multistage interferometers can be developed from off-the-shelf components and has the potential to detect very small amounts of analytes. The dynamic range, sensitivity, and detection limit of the sensor can be controlled by judicious choice of ratios of cavity lengths and/or increasing the number of FBGs. We anticipate that the present work will find wide usage in a variety of sensing applications in pharmaceutical, agriculture, and health care sectors.

Funding. Pakistan Science Foundation (PSF-TUBITAK/P-LUMS(03)).

Acknowledgment. The authors would like to thank Raja Ahmad, OFS Laboratories USA, for providing us useful suggestions to improve the manuscript.

REFERENCES

1. J. Liu, P. Jia, H. Zhang, X. Tian, H. Liang, Y. Hong, T. Liang, W. Liu, and J. Xiong, "Fiber-optic Fabry-Perot pressure sensor based on low-temperature co-fired ceramic technology for high-temperature applications," Appl. Opt. **57**, 4211–4215 (2018).
2. S. Liu, Y. Wang, C. Liao, G. Wang, Z. Li, Q. Wang, J. Zhou, K. Yang, X. Zhong, J. Zhao, and J. Tang, "High-sensitivity strain sensor based on in-fiber improved Fabry-Perot interferometer," Opt. Lett. **39**, 2121–2124 (2014).
3. H. Y. Choi, K. S. Park, S. J. Park, U.-C. Paek, B. H. Lee, and E. S. Choi, "Miniature fiber-optic high temperature sensor based on a hybrid structured Fabry-Perot interferometer," Opt. Lett. **33**, 2455–2457 (2008).

4. R. Wang and X. Qiao, "Gas refractometer based on optical fiber extrinsic Fabry-Perot interferometer with open cavity," IEEE Photon. Technol. Lett. **27**, 245–248 (2015).
5. C. Wang, G. Yan, Z. Lian, X. Chen, S. Wu, and S. He, "Hybrid-cavity Fabry-Perot interferometer for multi-point relative humidity and temperature sensing," Sens. Actuators B Chem. **255**, 1937–1944 (2018).
6. J. Mack, D. McNutt, F. Roesler, and R. Chabbal, "The PEPSIOS purely interferometric high-resolution scanning spectrometer. I. The pilot model," Appl. Opt. **2**, 873–885 (1963).
7. A. D. Gomes, M. Becker, J. Dellith, M. I. Zibaii, H. Latifi, M. Rothhardt, H. Bartelt, and O. Frazão, "Multimode Fabry-Perot interferometer probe based on Vernier effect for enhanced temperature sensing," Sensors **19**, 453 (2019).
8. Y. Zhao, P. Wang, R. Lv, and X. Liu, "Highly sensitive airflow sensor based on Fabry-Perot interferometer and Vernier effect," J. Lightwave Technol. **34**, 5351–5356 (2016).
9. P. Zhang, M. Tang, F. Gao, B. Zhu, Z. Zhao, L. Duan, S. Fu, J. Ouyang, H. Wei, P. P. Shum, and D. Liu, "Simplified hollow-core fiber-based Fabry-Perot interferometer with modified Vernier effect for highly sensitive high-temperature measurement," IEEE Photon. J. **7**, 1–10 (2015).
10. Y. Liu, Y. Li, M. Li, and J.-J. He, "High-sensitivity and wide-range optical sensor based on three cascaded ring resonators," Opt. Express **25**, 972–978 (2017).
11. H.-T. Kim and M. Yu, "Cascaded ring resonator-based temperature sensor with simultaneously enhanced sensitivity and range," Opt. Express **24**, 9501–9510 (2016).
12. T. Claes, W. Bogaerts, and P. Bienstman, "Experimental characterization of a silicon photonic biosensor consisting of two cascaded ring resonators based on the Vernier-effect and introduction of a curve fitting method for an improved detection limit," Opt. Express **18**, 22747–22761 (2010).
13. D. Dai, "Highly sensitive digital optical sensor based on cascaded high-q ring-resonators," Opt. Express **17**, 23817–23822 (2009).
14. H. Van de Stadt and J. M. Muller, "Multimirror Fabry-Perot interferometers," J. Opt. Soc. Am. A **2**, 1363–1370 (1985).
15. M. I. Cheema, C. Shi, A. M. Armani, and A. G. Kirk, "Optimizing the signal to noise ratio of microcavity sensors," IEEE Photon. Technol. Lett. **26**, 2023–2026 (2014).